Polarization patterns in Kerr media

Miguel Hoyuelos, Pere Colet, Maxi San Miguel, and Daniel Walgraef*
Instituto Mediterráneo de Estudios Avanzados, IMEDEA† (CSIC-UIB), Campus Universitat Illes Balears,
E-07071 Palma de Mallorca, Spain
(Received 17 November 1997)

We study spatiotemporal pattern formation associated with the polarization degree of freedom of the electric field amplitude in a mean field model describing a Kerr medium in a cavity with flat mirrors and driven by a coherent plane-wave field. We consider linearly as well as elliptically polarized driving fields, and situations of self-focusing and self-defocusing. For the case of self-defocusing and a linearly polarized driving field, there is a stripe pattern orthogonally polarized to the driving field. Such a pattern changes into a hexagonal pattern for an elliptically polarized driving field. The range of driving intensities for which the pattern is formed shrinks to zero with increasing ellipticity. For the case of self-focusing, changing the driving field ellipticity leads from a linearly polarized hexagonal pattern (for linearly polarized driving) to a circularly polarized hexagonal pattern (for circularly polarized driving). Intermediate situations include a modified Hopf bifurcation at a finite wave number, leading to a time dependent pattern of deformed hexagons and a codimension 2 Turing-Hopf instability resulting in an elliptically polarized stationary hexagonal pattern. Our numerical observations of different spatiotemporal structures are described by appropriate model and amplitude equations. [S1063-651X(98)12608-9]

PACS number(s): 05.45.+b, 47.54.+r, 42.65.Wi, 42.65.Sf

I. INTRODUCTION

Spatiotemporal patterns in the transverse direction of an optical field are now being widely studied theoretically and experimentally [1]. In particular, the nonlinear optical configuration of a thin slice of Kerr material with a single feedback mirror analyzed in Ref. [2] is the basis of many results recently obtained in this field. Studies of optical pattern formation share a number of aspects and techniques with general investigations of pattern formation in other physical systems [3], but they also have specific features such as the role of light diffraction. A special feature of light patterns comes from the vectorial degree of freedom associated with the polarization of the light electric field amplitude. A vectorial degree of freedom also appears in recent studies of two-component Bose-Einstein condensates [4] modeled by coupled nonlinear Schrödinger equations. Consideration of this degree of freedom opens the way to study a rich variety of *vectorial* spatiotemporal phenomena. However, in many studies of optical pattern formation, this extra degree of freedom has not been taken into account. Those studies correspond to situations in which a linear polarization of light is well stabilized. We will refer to these situations of frozen polarization as the ''scalar case.'' An early study of polarization dynamical instabilities in nonlinear optics was done in Ref. [5]. For a review on polarization instabilities and multistability, see, Ref. [6]. Space independent polarization instabilities have also been studied in lasers [7–10]. More recently, vectorial patterns associated with polarization instabilities have been considered in lasers [11–17] as well as in nonlinear passive optical media. For this latter case, new types of vectorial instabilities have been predicted for cavity [18] or single feedback mirror [19] systems. Several experiments in cells with alkaline vapors have been reported either without an optical cavity [20,21] or with a single feedback mirror [22,23]. Dynamically evolving patterns produced in a cell of rubidium vapor with counterpropagating beams have also been studied experimentally [24]. Within this context of recent experimental studies, in this paper we address several aspects of polarization transverse patterns and pattern dynamics in passive optical systems, presenting a systematic study of a model system.

Pattern formation in nonlinear cavities for the scalar case was already considered in Ref. [25]. A prototype simple model which has been very useful for the understanding of pattern formation in this case is a mean field model describing a Kerr medium in a cavity with flat mirrors and driven by a coherent plane-wave field [26,27]. This model was extended in Refs. [18,28] to take into account the polarization degrees of freedom. Even if a Kerr material model does not give a faithful description of alkali vapors, it shares with them some basic polarization mechanisms of pattern formation. In addition, the relative simplicity of the model in Ref. [18] makes it worthwhile to study it in depth as a general prototype model for the basic understanding of vectorial patterns. Here we undertake such a study, going beyond the situations already considered in Ref. [18]. The study in Ref. [18] was limited to the case in which the driving field is linearly polarized. Allowing for an elliptically polarized driving field, as we do here, gives rise to a rich variety of new phenomena. In addition, the role of elliptically polarized homogeneous solutions in a number of pattern forming instabilities is discussed in detail. Those solutions already exist in the case of a linearly polarized driving field.

Our study involves a combination of linear stability analysis, numerical simulations, and amplitude and model equa-

*Permanent address: Center for Nonlinear Phenomena and Complex Systems, Université Libre de Bruxelles, Campus Plaine, Boulevard du Triomphe Boîte Postale 231, 1050 Bruxelles, Belgium.
†URL: http://www.imedea.uib.es/PhysDept.

tions. Guided by the results of linear stability analysis, we search numerically for different spatiotemporal structures. The general features of these structures are then shown to be described by model and amplitude equations which are justified by general arguments of symmetry, the form of the linear instability, and the identification of relevant nonlinear couplings.

The paper is organized as follows: In Sec. II we describe the model we are considering, its spatially homogeneous solutions, and general properties of the stability analysis of these states. In Sec. III we consider the case of a linearly polarized driving field, while in Sec. IV we discuss the case of an elliptically polarized driving field. Two particular situations of this last case are considered in the two following sections. Section V is devoted to describing the deformed dynamical hexagons occurring in a modified Hopf bifurcation, and Sec. VI discusses the Turing-Hopf codimension 2 bifurcation. A summary of results and their connection with related studies is given in Sec. VII. Finally, some general concluding remarks are given in Sec. VIII.

II. DESCRIPTION OF THE MODEL, REFERENCE STEADY STATES, AND STABILITY ANALYSIS

The system we consider is a Fabry-Pérot or ring cavity filled with an isotropic Kerr medium. The cavity is driven by an external input field of arbitrary polarization. The situation in which the polarization degree of freedom of the electromagnetic field is frozen was first considered by Lugiato and Lefever [26] and Firth *et al.* [27]. Geddes *et al.* [18] generalized the model of Ref. [26] to allow for the vector nature of the field. Their description of this system is given by a pair of coupled equations for the evolution of the two circularly polarized components of the field envelope E_+ and E_-, defined by

$$E_\pm = \frac{1}{\sqrt{2}}(E_x \pm iE_y).$$

For an isotropic medium, the equations are

$$\frac{\partial E_\pm}{\partial t} = -(1+i\eta\theta)E_\pm + ia\nabla^2 E_\pm + E_{0\pm} + i\eta[A|E_\pm|^2 + (A+B)|E_\mp|^2]E_\pm, \quad (1)$$

where $E_{0\pm}$ are the circularly polarized components of the input field, $\eta=+1(-1)$ indicates self-focusing (self-defocusing), θ is the cavity detuning, a represents the strength of diffraction, and ∇^2 is the transverse Laplacian. A and B are parameters related to the components of the susceptibility tensor. As here we are considering an isotropic medium, $A+B/2=1$ $(B\leqslant 2)$.

The case in which $E_{0+}=E_{0-}$ was considered in Ref. [18], and corresponds to a linearly polarized input field. Here we consider an input field with arbitrary ellipticity χ, defined as

$$E_{0+} = \sqrt{I_0}\cos(\chi/2), \qquad E_{0-} = \sqrt{I_0}\sin(\chi/2), \quad (2)$$

where I_0 is the intensity of the input field. We consider that E_{0+} and E_{0-} are real. This assumption fixes the main axis of the ellipse in the X or Y direction. Note that $\chi=\pi/2$ corresponds to linear polarization along the X axis, and that the ellipticity increases when the value of χ is changed from this value. $\chi=0$ $(\chi=\pi)$ corresponds to a right-handed (left-handed) circularly polarized input field. Finally, $\chi=-\pi/2$ corresponds to linear polarization along the Y axis. The intensities of the circularly polarized components of the input field are $I_{0+}=I_0\cos^2(\chi/2)$ and $I_{0-}=I_0\sin^2(\chi/2)$. We note that the case of a scalar field considered in Refs. [26,27] is formally recovered from Eq. (1) for a circularly polarized input. The circular component of the field which is not excited by the input field decays to zero, and the equation for the other component coincides with the one in Ref. [26] up to a rescaling of the field amplitude.

The steady state homogeneous solutions of Eq. (1) are reference states from which transverse patterns emerge as they become unstable. These patterns are described in the following sections for different situations. The steady state homogeneous solutions $E_{s\pm}$ are given by the implicit equation

$$E_{0\pm} = E_{s\pm}\left\{1 - i\eta\left[\left(1-\frac{B}{2}\right)I_{s\pm} + \left(1+\frac{B}{2}\right)I_{s\mp} - \theta\right]\right\}, \quad (3)$$

where $I_{s\pm}=|E_{s\pm}|^2$. For the intensities we have

$$I_{0\pm} = I_{s\pm}\left\{1 + \left[\left(1-\frac{B}{2}\right)I_{s\pm} + \left(1+\frac{B}{2}\right)I_{s\mp} - \theta\right]^2\right\}. \quad (4)$$

This gives a pair of coupled cubic polynomials in I_{s+} and I_{s-}. Solving for I_{s+} and I_{s-} leads to a polynomial of degree 9 from which it is not possible, in principle, to find an analytical expression.

For the particular case of linearly polarized input field, Eq. (4) admits symmetric $(I_{s+}=I_{s-}=I_s)$ and asymmetric $(I_{s+}\neq I_{s-})$ solutions. The symmetric solution corresponds to linearly polarized output light, while the asymmetric is elliptically polarized. For the symmetric solution Eq. (4) reduces to the single equation [29]

$$I_0/2 = I_s[1+(2I_s-\theta)^2], \quad (5)$$

which gives an implicit formula for I_s. As it is well known, Eq. (5) implies bistability for $\theta>\sqrt{3}$. We will restrict our analysis to nonbistable regimes, i.e. $\theta<\sqrt{3}$. The asymmetric solution is obtained from the general equation (4). This solution breaks the $(+,-)$ symmetry of the problem and is degenerate. There is one solution with $I_{s+}>I_{s-}$, and a second equivalent solution in which I_{s+} and I_{s-} are interchanged. The asymmetric solution only exists for values of I_0 greater than a threshold value for which $I_{s+}=I_{s-}=I'$. An

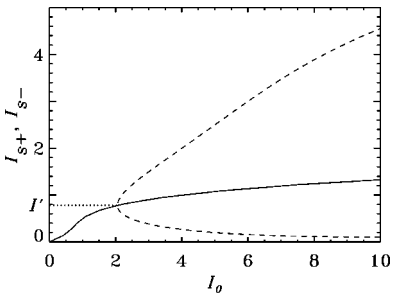

FIG. 1. Steady state homogeneous solutions, as a function of the input field intensity, for linearly polarized light, $\chi=90°$. The solid line is the symmetric solution. The dashed line corresponds to the asymmetric solutions. The two branches of the asymmetric solution give the values of I_{s+} and I_{s-} in one of the two degenerate solutions, and they meet the symmetric solution for $I_{s+}=I_{s-}=I'$. Parameter values: $a=1$, $B=1.5$, and $\theta=1$. These parameter values are the same for all the figures, except where otherwise noticed. The quantities plotted in all the figures are dimensionless.

example of the symmetric and asymmetric solutions for linearly polarized input is given in Fig. 1. The value of I' is given by

$$I'=\frac{\theta(B-2)+\sqrt{\theta^2B^2+4(B-1)}}{4(B-1)}. \tag{6}$$

For circularly polarized input light, for example $\chi=0$, Eq. (4) reduces to

$$I_0=I_{s+}\left\{1+\left[\left(1-\frac{B}{2}\right)I_{s+}-\theta\right]^2\right\}, \tag{7}$$

and $I_{s-}=0$. It is clear from Eqs. (5) and (7) that the solution for a circularly polarized input is the same as the symmetric solution for a linearly polarized input, up to a rescaling of the intensities.

An elliptically polarized input breaks the $(+,-)$ symmetry of the system. The symmetric solution (5) found for linearly polarized input no longer exists. Instead there is a single asymmetric solution (4) which favors the ellipticity of the input field. When the ellipticity of the input field is decreased, this solution approaches the asymmetric solution obtained for a linearly polarized input. An example of this homogeneous elliptically polarized solution, obtained from Eq. (4), is shown in Fig. 2 for various values of the ellipticity of the input field. This solution favors I_{s+}, and an equivalent solution favoring I_{s-} is found when the ellipticity is changed from χ to $\pi-\chi$.

Basic features of the stability of the steady state homogeneous solutions can be analyzed by considering the evolution equations for perturbations $\psi_\pm$ defined by

$$E_\pm=E_{s\pm}[1+\psi_\pm]. \tag{8}$$

From Eqs. (1) and (8), we find

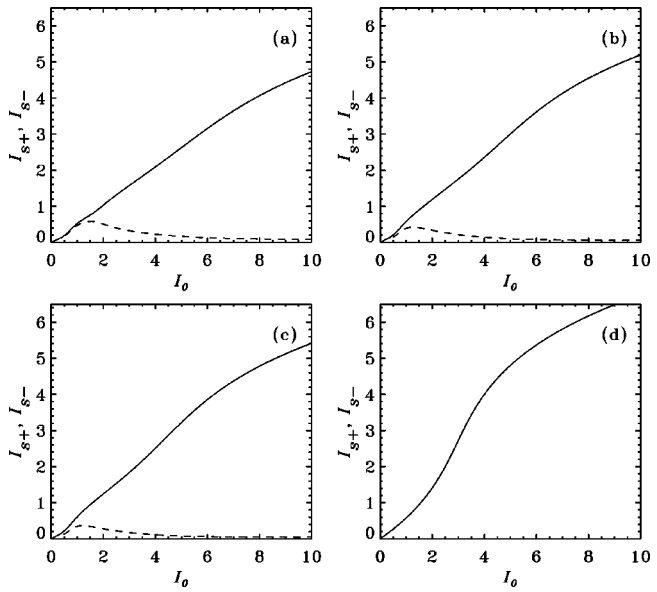

FIG. 2. Steady state solutions for different values of the ellipticity χ of the input field. The solid lines correspond to the value of I_{s+}, and the dashed lines to I_{s-}. Input field ellipticity values: (a) $\chi=87°$, (b) $\chi=78°$, (c) $\chi=73°$, and (d) $\chi=0°$. Note that $I_{s-}=0$ in (d).

$$\begin{aligned}\partial_t\psi_\pm=&-\left[1+i\eta\left(\theta-S\pm\frac{BR}{2}\right)-ia\nabla^2\right]\psi_\pm\\&+i\eta\frac{S}{2}\left[\left(1-\frac{B}{2}\right)(\psi_\pm+\psi_\pm^*+|\psi_\pm|^2)\right.\\&\left.+\left(1+\frac{B}{2}\right)(\psi_\mp+\psi_\mp^*+|\psi_\mp|^2)\right](1+\psi_\pm)\\&\pm i\eta\frac{R}{2}\left[\left(1-\frac{B}{2}\right)(\psi_\pm+\psi_\pm^*+|\psi_\pm|^2)\right.\\&\left.-\left(1+\frac{B}{2}\right)(\psi_\mp+\psi_\mp^*+|\psi_\mp|^2)\right](1+\psi_\pm),\end{aligned} \tag{9}$$

with

$$I_{s\pm}=\frac{1}{2}(S\pm R). \tag{10}$$

The parameter R measures the deviation from a symmetric solution vanishing for linearly polarized solutions.

It is convenient to make a change of variables to the following basis [18]:

$$\Sigma=\begin{Bmatrix}\sigma_1\\\sigma_2\\\sigma_3\\\sigma_4\end{Bmatrix}=\begin{Bmatrix}\mathrm{Re}(\psi_++\psi_-)\\\mathrm{Im}(\psi_++\psi_-)\\\mathrm{Re}(\psi_+-\psi_-)\\\mathrm{Im}(\psi_+-\psi_-)\end{Bmatrix}. \tag{11}$$

In this basis, which emphasizes the role of symmetric ($\psi_+=\psi_-$) and antisymmetric ($\psi_+=-\psi_-$) modes, Eq. (9) may be written as:

$$\partial_t\Sigma=L\Sigma+N_2(\Sigma|\Sigma)+N_3(\Sigma|\Sigma|\Sigma), \tag{12}$$

where the linear matrix (in Fourier space) is

$$L=\begin{pmatrix} -1 & -\eta(S-\theta_k) & 0 & \eta BR/2 \\ \eta(3S-\theta_k) & -1 & -\eta(B/2-2)R & 0 \\ 0 & \eta BR/2 & -1 & -\eta(S-\theta_k) \\ -3\eta BR/2 & 0 & \eta(S(1-B)-\theta_k) & -1 \end{pmatrix}, \tag{13}$$

with

$$\theta_k=\theta+\eta a k^2. \tag{14}$$

The structure of the linear matrix is particularly simple for a symmetric solution $R=0$ [18]: L becomes a matrix with 2×2 blocks in which the symmetric and antisymmetric modes are decoupled. As a consequence, the linear instabilities lead to the growth of either a symmetric or an antisymmetric mode (see Sec. III). The eigenvalues λ of L are

$$\begin{aligned} \lambda_{1,2}&=-1\pm\sqrt{(\theta_k-3S)(S-\theta_k)}, \\ \lambda_{3,4}&=-1\pm\sqrt{(\theta_k+(B-1)S)(S-\theta_k)}. \end{aligned} \tag{15}$$

In the general case of elliptically polarized input, the linear unstable modes are not purely symmetric or antisymmetric. The general expression for the four independent eigenvalues of L are

$$\begin{aligned} \lambda_{1,2,3,4}&=-1\pm\tfrac{1}{2}\sqrt{f_1\pm\sqrt{f_2}}, \\ f_1&=(2B-8)S^2-2\theta_k(B-6)S-2B(B-1)R^2-4\theta_k^2, \\ f_2&=4(B+2)^2S^2(S-\theta_k)^2 \\ &\quad -4B(5B^2-16B+20)R^2S^2 \\ &\quad +12\theta_kB(B-2)(B-6)R^2S+B^2(B+2)^2R^4 \\ &\quad +32B\theta_k^2(B-2)R^2. \end{aligned} \tag{16}$$

The different eigenvalues correspond to the four different combinations of plus and minus signs in the square roots. Replacing the values of R and S, the eigenvalues are given as functions of the steady state intensities I_{s+} and I_{s-}. Their dependence on η is implicit in θ_k. A given homogeneous steady state solution (I_{s+},I_{s-}) becomes unstable when the real part of one eigenvalue becomes positive. These instabilities are described in detail in Sec. III for linearly polarized input, and in Sec. IV for the general case of elliptically polarized input.

The nonlinearities in Eq. (12) include quadratic $[N_2(\Sigma|\Sigma)]$ and cubic $[N_3(\Sigma|\Sigma|\Sigma)]$ terms. The structure of these terms also gives some general information on the nature of the instabilities. In particular, if the quadratic nonlinearity $N_2(\Sigma|\Sigma)$ does not vanish, one expects the formation of hexagonal patterns instead of stripes. In addition, a stationary instability (which corresponds to a purely real eigenvalue becoming positive) is expected to be subcritical.

For the symmetric solution $(R=0)$, the quadratic nonlinearity is given by

$$N_2^S(\Sigma|\Sigma)=\frac{\eta S}{2}\begin{Bmatrix} B\sigma_3\sigma_4-2\sigma_1\sigma_2 \\ 3\sigma_1\sigma_1+\sigma_2\sigma_2+(1-B)\sigma_3\sigma_3+\sigma_4\sigma_4 \\ B\sigma_2\sigma_3-2\sigma_1\sigma_4 \\ 2(1-B)\sigma_1\sigma_3-B\sigma_2\sigma_4 \end{Bmatrix}. \tag{17}$$

Inspection of $N_2^S(\Sigma|\Sigma)$ shows that quadratic nonlinearities, and therefore hexagonal pattern formation, are only expected for an instability of the symmetric mode. In this case, the critical modes are linear combinations of the modes σ_1 and σ_2, and $N_2^S(\Sigma|\Sigma)$ plays an important role since the first two components contains products of two unstable modes. Alternatively, if an asymmetric mode becomes unstable, the critical modes are linear combinations of σ_3 and σ_4. The third and fourth components of the vector $N_2^S(\Sigma|\Sigma)$ contain products of one stable mode and one unstable mode, but no products of two unstable modes. The adiabatic elimination of the stable modes yields quadratic terms involving two unstable modes, but these are terms of higher order and can be neglected.

For an elliptically polarized solution, there is an additional contribution to the quadratic nonlinearity N_2; we find

$$N_2(\Sigma|\Sigma)=N_2^S(\Sigma|\Sigma)+\frac{\eta R}{4}M_2(\Sigma|\Sigma), \tag{18}$$

where

$$M_2(\Sigma|\Sigma)=\begin{Bmatrix} 2B\sigma_1\sigma_4-4\sigma_2\sigma_3 \\ 2(4-B)\sigma_1\sigma_3+4\sigma_2\sigma_4 \\ 2B\sigma_1\sigma_2-4\sigma_3\sigma_4 \\ -3B\sigma_1\sigma_1+(4-B)\sigma_3\sigma_3-B(\sigma_2\sigma_2+\sigma_4\sigma_4) \end{Bmatrix}. \tag{19}$$

Therefore, even for a purely asymmetric unstable mode there are important quadratic contributions which involve the unstable modes ($\sigma_3\sigma_3$, $\sigma_3\sigma_4$, and $\sigma_4\sigma_4$), and hexagonal pattern formation is generally expected.

III. LINEARLY POLARIZED INPUT FIELD

In this section we discuss transverse polarization patterns in the case of a linearly polarized input field, which we take to be X polarized. We have found (see Fig. 1) two types of homogeneous steady state solutions: a symmetric solution that is also X polarized, and an asymmetric one. The marginal stability curve for each solution is obtained from the eigenvalues of the matrix L given in Eqs. (15) and (17).

We first consider the stability properties of the solutions

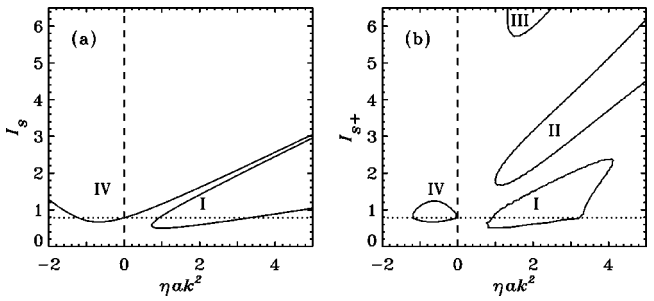

FIG. 3. Marginal stability curves for linearly polarized input field as described in the text: (a) stability of the symmetric solution and (b) stability of symmetric solution (up to I') and asymmetric solution. The dotted line displays the value of I'. The vertical dashed line separates the self-focusing case (to the right) from the self-defocusing one (left).

with respect to homogeneous perturbations. The symmetric solution becomes unstable for a zero wave number perturbation ($k=0$) for $I_s=I'$. This is the point where the asymmetric solution appears. For $I_s>I'$, the asymmetric solution is stable with respect to homogeneous perturbations.

Finite wave number perturbations destabilize the symmetric solution for $I_s<I'$ and the asymmetric solution for $I_s>I'$. In Fig. 3, we plot marginal stability curves for $\theta=1$ as a function of ηak^2, so that positive values of this parameter correspond to self-focusing and negative values to self-defocusing. Figure 3(a) shows the marginal stability curve for the symmetric solution [18]. For the symmetric solution, the shape of the marginal stability curves is, in fact, the same for any value of the detuning θ. This is because the eigenvalues λ_i given by Eq. (15) depend only on θ_k and $S=2I_s$, so a change in the value of θ is equivalent to a displacement of the origin of ηak^2 (vertical dashed line) by the same amount. The vertical dashed line separating the self-focusing and self-defocusing cases moves to the right if the detuning θ is increased, and it intersects the left corner of region I for $\theta=\sqrt{3}$ (the value of θ beyond which there is bistability). Since in this paper we are only considering the nonbistable regime, the vertical dashed line is always situated to the left of region I.

Figure 3(b) shows marginal stability curves for the asymmetric solution which merge continuously with the marginal curves of the symmetric solution for $I_s<I'$. In this case, the eigenvalues λ_i given by Eq. (16) depend on θ_k and S, and also on R. As S and R are related by the steady state solution (4) which depends explicitly on θ, the shape of the marginal stability curves changes slightly for different values of θ.

For values of θ in the range $2/B-1<\theta<\sqrt{3}$, the situation is similar to the case shown in Figs. 3(a) and 3(b). The homogeneous symmetric (linearly polarized) solution is stable for low values of the input or the field intensity, and it becomes unstable to finite wave number perturbations for values of $I_s<I'$. The marginal stability curves for the symmetric solution intersect the $k=0$ vertical axis at $I_s=I'$, in agreement with the analysis of homogeneous perturbations mentioned above. This analysis also implies that there is no instability along the vertical axis $k=0$ for the asymmetric solution Fig. 3(b). The analysis of the instability thresholds that arise by increasing the input intensity is the same in both Figs. 3(a) and 3(b), with the threshold being lower for the self-focusing case than for the self-defocusing case. However, as shown in Fig. 3(b), for the self-defocusing case the region of instability IV is now reduced to an island, so that further above this threshold an homogeneous elliptically polarized solution is stable. Given that there is no instability along the vertical axis $k=0$ in Fig. 3(b), the island IV extends around its minima until it tangentially touches the vertical axis at $k=0$. If θ is decreased, the vertical axis moves to the left, and the size of the island IV becomes smaller until it disappears for $\theta=2/B-1$.

No regions of stability are found above I' in Fig. 3(b) for the self-focusing case. The different instability islands and tongues found here will turn out to be a useful guide for analyzing the stability of the homogeneous solution for an elliptically polarized input. We recall that such a solution appears continuously from the asymmetric solution analyzed here. In particular, the instability tongue in the middle, labeled II, is associated with an eigenvalue with a nonvanishing imaginary part, and, therefore, it identifies a possible Hopf bifurcation at a finite wave number.

It is possible to perform a weakly nonlinear analysis to predict the kind of pattern that emerges at threshold. The structure of the amplitude equations may be easily obtained either in the self-focusing or self-defocusing case. In the self-defocusing case (the negative part of the horizontal axis in Fig. 3), the homogeneous symmetric solution becomes unstable for $I^c_{s\pm}=1/B$, and the critical wave number is given by $ak_c^2=\theta+1-2/B$. The instability is stationary and supercritical, and it comes from the σ_3,σ_4 box of the linear matrix L in Eq. (13), so that the critical mode is an antisymmetric mode of zero frequency. As discussed in Sec. II, this implies that quadratic nonlinearities are not important, and stripe patterns are expected. The amplitude equation of the stripe pattern was presented in Ref. [18]. Given the antisymmetric nature of the unstable mode, the X-polarized component of the field is stable and remains homogeneous, while the stripe pattern appears in the Y-polarized component, which has a zero value below the instability. Overall, the electric field displays an elliptically polarized spatial structure. We remark that such an instability is of a purely vectorial nature, with no analog when the polarization degree of freedom is frozen. In fact, no pattern formation instability occurs in this case for a self-defocusing medium.

In Fig. 4, we give an example of this polarization pattern instability [30], showing a sequence of plots of $|E_+|^2$ for increasing values of the input field. The first plot corresponds to a situation close to threshold where the stripe pattern emerges. The snapshots shown correspond to long lived transient states that evolve to an ordered stripe pattern by defect evolution and annihilation. In the last plot, the input intensity is such that the homogeneous asymmetric state is stable, since we are outside the island of instability in Fig. 3(b). The system segregates into two phases which correspond to the two equivalent homogeneous elliptically polarized solutions. The evolution of the system at later times is dominated by the motion of the interfaces separating the two stable phases.

For the self-focusing case (the positive part of the horizontal axis in Fig. 3), the homogeneous symmetric solution becomes unstable for $I^c_{s\pm}=\frac{1}{2}$, with a critical wave number given by $ak_c^2=2-\theta$. The instability is also stationary, but it

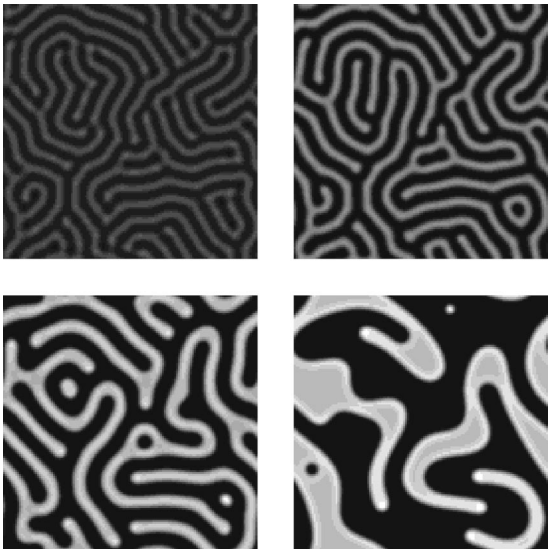

FIG. 4. Plots of $|E_+|^2$ for increasing values of the intensity of the linearly polarized input field in the self-defocusing case ($\eta=-1$). From left to right and top to bottom, $I_{s+}=0.8$ ($I_0=1.8$), $I_{s+}=1.5$ ($I_0=3.1$), $I_{s+}=2.6$ ($I_0=5.1$), and $I_{s+}=3.0$ ($I_0=6.0$). Gray scale values: black, 0.1; white, 3.8.

now comes from the σ_1,σ_2 box of the linear matrix L in Eq. (13) [18]. The critical mode is therefore a symmetric mode. In this case, quadratic nonlinearities are present, and, as discussed in Sec. II, one then expects the formation of hexagonal patterns via a subcritical bifurcation. Such hexagonal patterns are shown in Fig. 5. The situation corresponds to the case discussed in Ref. [27], in which the polarization degree of freedom is not taken into account. The instability leads to an *X*-polarized pattern, while the *Y*-polarized component of the field continues to be zero. If the intensity is further increased, the hexagonal structure is disarranged [31]. In this case, the state of the system is far away from the steady state solution, so the marginal stability plots of Fig. 3 are no longer useful. We observe a spatiotemporal dynamics in which the intensity of the hexagonal peaks grow, leading to high intensity localized structures placed randomly. These structures eventually burst, producing circular waves that propagate in the transverse plane and dissipate away (see Fig. 5). In the two-dimensional self-focusing nonlinear Schrödinger equation, there is a phenomenon of wave collapse [32]. Collapse is known to be prevented by dissipation [33] or by a saturation nonlinearity [32]. In our problem, we have dissipation and a driving field. We have checked that the same phenomenon appears when our cubic nonlinearity is replaced by a saturating nonlinearity. What we then observe is a strong effect of self-focusing in a situation with no collapse.

We finally consider the range of detuning values $\theta\leqslant 2/B-1$. In this range, the vertical dashed line $k=0$ is at the left of the minimum of region IV in Fig. 3(a). In the equivalent of Fig. 3(b) for these values of θ, the island IV appears to the right of the vertical axis $k=0$ and extends around its minimum, located at $ak_c^2=-\theta-1+2/B$, until it tangentially touches the vertical axis $k=0$. According to this picture, in the self-defocusing case the linearly polarized homogeneous solution becomes unstable at $I_s=I'$ to $k=0$ perturbations,

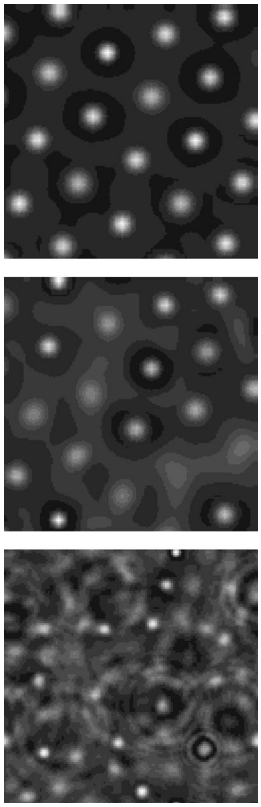

FIG. 5. Plots of $|E_+|^2$ for increasing values of the input field in the self-focusing regime ($\eta=1$). In this figure the gray scale is logarithmic. From top to bottom, $I_{s+}=0.48$ ($I_0=0.96$; black, 0.16; white, 3.5), $I_{s+}=0.55$ ($I_0=1.1$; black, 0.0018; white, 9.8) and $I_{s+}=1.7$ ($I_0=3.2$; black, 0.0028; white, 17).

leading to an elliptically polarized homogeneous solution with no pattern being formed. In the self-focusing case, the situation is very similar to the one described before for $2/B-1<\theta<\sqrt{3}$. Although region IV is now located in the self-focusing region, it does not contribute to the instability scenario, since its minimum value ($I^c_{s\pm}=1/B$) is above the minima of region I ($I^c_{s\pm}=\frac{1}{2}$). So, as the input field intensity is increased, the homogeneous symmetric solution becomes unstable for $I^c_{s\pm}=\frac{1}{2}$, with a critical wave number given by $ak_c^2=2-\theta$, and a hexagonal pattern is formed via a subcritical bifurcation. For the particular limiting value $B=2$, the minimum of the region IV is located at the same value as the minimum of region I. These two instability regions are associated with real eigenvalues, so they identify two stationary (Turing-like) bifurcations. So, for $B=2$ and $\theta\leqslant 2/B-1=0$, starting from the linearly polarized homogeneous solution, as the input field is increased the system crosses the two instability thresholds simultaneously. This is a codimension 2 bifurcation involving two stationary modes. The critical mode associated to region I is symmetric and has a critical wave number $ak_c^2=2-\theta$, while a critical mode associated with region IV is asymmetric and has a critical wave number $ak_c^2=-\theta$ [57].

IV. ELLIPTICALLY POLARIZED INPUT FIELD

In this section we present a general description of the stability analysis of the stationary state when the input field

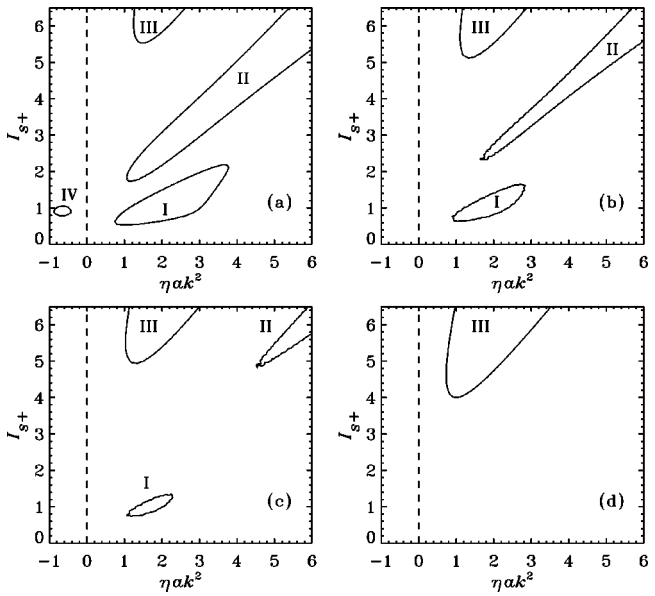

FIG. 6. Marginal stability curves for the same values of the ellipticity χ of the input field as in Fig. 2: (a) $\chi=87°$, (b) $\chi=78°$, (c) $\chi=73°$, and (d) $\chi=0°$.

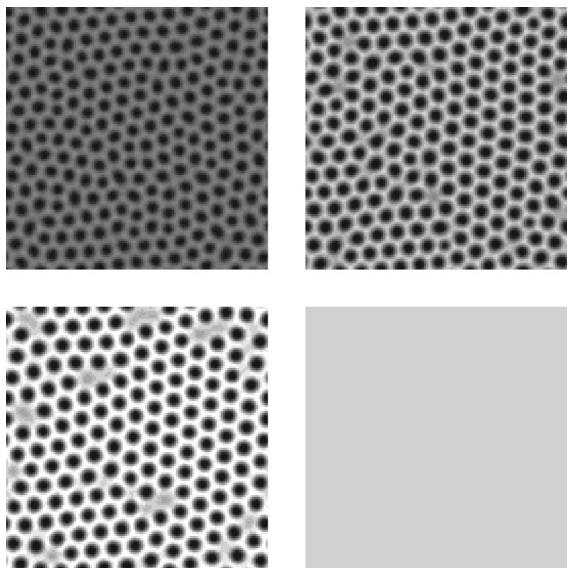

FIG. 7. $|E_+|^2$ for increasing values of the quasilinearly polarized input field ($\chi=87°$) in the self-defocusing case ($\eta=-1$). From left to right and from top to bottom, $I_{s+}=0.8$ ($I_0=1.8$), $I_{s+}=1.7$ ($I_0=3.1$), $I_{s+}=2.1$ ($I_0=3.8$), and $I_{s+}=2.3$ ($I_0=4.2$). Gray scale values: black, 0.13; white, 2.6.

is elliptically polarized. Throughout this section, we are considering a detuning $\theta=1$. Figure 6 shows, for different input field ellipticities χ, the marginal stability curve obtained introducing the stationary solution (4) in Eq. (16) and solving $\mathrm{Re}(\lambda)=0$.

For a small input field intensity, when the ellipticity is small, the homogeneous solution is close to the symmetric solution for a linearly polarized input field, so that $R \ll S$. The eigenvalues λ of the linear evolution matrix given in Eq. (17) can be expanded as a series in R^{2n} in the form

$$\lambda_i=\lambda_i^0+\lambda_i^1 R^2, \tag{20}$$

where λ_i^0 are the eigenvalues for the case of the purely linearly polarized input field $\chi=\pi/2$. Thus the instability thresholds displayed in Fig. 6(a) for $\chi=87°$ are very similar to the ones of Fig. 3(a), corresponding to the symmetric solution of the linearly polarized input field. For a larger input field and small ellipticity, the homogeneous solution is close to the asymmetric solution for a linearly polarized input field, and the marginal stability curves shown in Fig. 6(a) are very similar to the ones of Fig. 3(b).

In the self-defocusing case (the negative part of the horizontal axis of Fig. 6), the size of the instability region of the homogeneous solution is decreased as the ellipticity is increased. For a large enough ellipticity, this instability island disappears, and the elliptically polarized homogeneous solution is always stable [see Figs. 6(b) and 6(c)]. For small ellipticity, the critical modes are basically combinations of the antisymmetric modes σ_3 and σ_4. Despite smallness of the corrections in the eigenvalues and the eigenvectors, the nonlinear terms in the amplitude equation are modified. The quadratic terms $N_2(\Sigma|\Sigma)$ now contain products of the two unstable modes through $M_2(\Sigma|\Sigma)$ [see Eqs. (18) and (19)]. As discussed in Sec. II, these terms should induce the formation of hexagonal rather than stripe patterns (as was the case for linear polarization of the input field), at least close to threshold [3,34]. The formation of hexagonal patterns rather than stripes due to the presence of small ellipticities in the input field has been experimentally observed in rubidium vapor [24]. Since the quadratic terms are proportional to R, the range of stability of hexagonal planforms should be proportional to R^2 [3,35]. In principle, in this situation, on increasing the bifurcation parameter (input field intensity), hexagons should become unstable and stripes should be observed [35]. However, due to the small size of the island where the homogeneous solution is unstable, when increasing the input field intensity we never found a stripe pattern in our simulations. Instead, we have a transition back to the elliptically polarized homogeneous state which is stable. In Fig. 7, we present a sequence of plots of $|E_+|^2$ for increasing values of the input intensity. Near threshold we have hexagons, and, for a large enough intensity, the homogeneous solution is restored. Different from the case of a linearly polarized input, here there is no competition between two phases with dominant E_+ or E_-, because the small ellipticity that we have introduced makes the system choose the solution with $I_{s+}>I_{s-}$. Since the quadratic nonlinearities are proportional to R, the sign of R should determine if the hexagons are of the 0 or π type [23,35,36]. As the dynamical evolution of the perturbations ψ_+ and ψ_- is associated with $\pm R$ [Eq. (9)], we find the opposite type of hexagons for $|E_+|^2$ and $|E_-|^2$. Changing the ellipticity χ to $\pi-\chi$ induces a transition, for a given circularly polarized component of the field, from one type of hexagons to the other, similarly to what was reported in Ref. [23]. We also note that, near threshold, the hexagonal pattern looks different if we consider the X or Y components of the field. In Fig. 8, we plot $|E_x|^2$ and $|E_y|^2$, for which we find hexagonal pattern of the ''black eye'' type. Similar patterns have been observed in chemical systems [37]. Here they arise because of the superposition of E_+ and E_-.

In the self-focusing case (the positive part of the horizon-

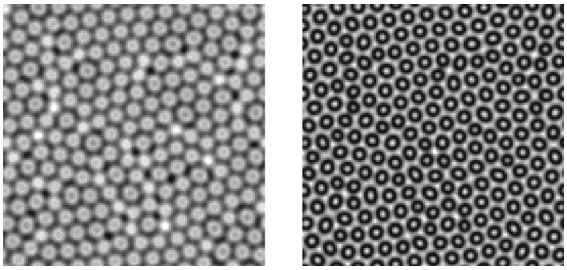

FIG. 8. $|E_x|^2$ (left figure: black, 1.2; white, 1.5) and $|E_y|^2$ (right figure: black, 0; white, 0.58) for $I_{s+}=0.8$ ($I_0=1.8$). The values of the other parameters are the same as in Fig. 7.

tal axis of Fig. 6), and for small ellipticity, the islands and tongues of instability of the homogeneous solution are obtained continuously from the ones for the asymmetric solution of linearly polarized input field [Fig. 3(b)]. Island I in Fig. 6(a) corresponds to a stationary instability of the modes which by continuity go to the symmetric modes when $R \rightarrow 0$. As there are quadratic terms in the amplitude equation, a hexagonal pattern is formed, similarly to the case of a linearly polarized input field. Tongues II and III are far away from the threshold for instability of the homogeneous solution, and are plotted in this figure only to display how they move as we increase the ellipticity. As in the case of linear polarization of the input field, tongue II is associated with a Hopf bifurcation, and tongue III with a stationary instability.

Figure 6(b) shows the marginal stability curve for $\chi=78°$. When the input field intensity is increased starting from zero, we have, as usual, a first instability of the Turing type, where a hexagonal structure emerges. The instability island I is now smaller, and there is a window for I_{s+} around 2, where the elliptically polarized homogeneous solution is stable. By further increasing the input field intensity, a second instability appears when the value of I_{s+} crosses the instability threshold of tongue II. The corresponding eigenvalues of the linear evolution matrix have nonzero imaginary parts, and cross the imaginary axis at a finite wave number, so that this instability is a Hopf bifurcation with broken space translational symmetry. This situation is discussed in detail in Sec. V.

As we can see from the sequence of plots in Fig. 6, tongue II moves upward and the tongue III downward as the ellipticity of the input field is increased (χ is decreased). Beyond the island of instability I, the patterns that are expected to form depend crucially on the relative position of the Hopf instability (tongue II) and the stationary instability of tongue III. When the stationary instability is the first to appear on increasing the bifurcation parameter, a steady spatial structures may be expected. If the Hopf bifurcation is the first to appear, however, one should obtain wavy spatiotemporal structures. If both instabilities are at the same level, one has a codimension 2 situation, as shown in Fig. 6(c) for $\chi=73°$. With respect to the situation of Fig. 6(b), instability tongue II has moved upward and to the right, while tongue III has moved downward, on until the instabilities associated with each of the two tongues take place at the same value of I_{s+}. There is now a large range of values of I_{s+} between the island I and the two tongues for which the elliptically polarized homogeneous solution is stable. Increasing I_{s+} from a value in this range, the homogeneous state has a codimension 2 bifurcation where steady and wavy modes should interact, ending with pure Turing, pure Hopf, or mixed modes, according to their nonlinear interaction. This case is discussed in more detail in Sec. VI.

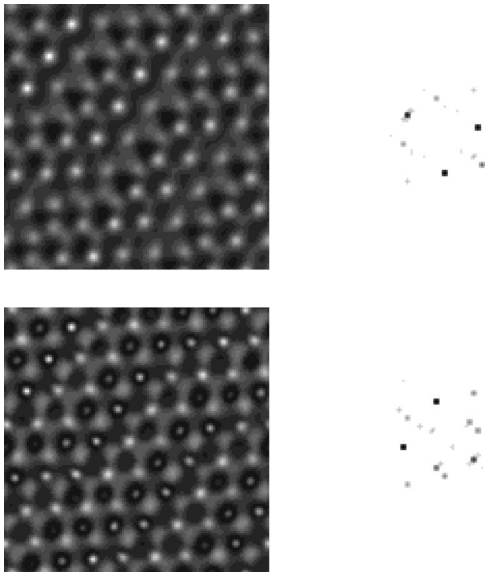

FIG. 9. From left to right and top to bottom, $|E_+(x,y)|^2$ (near field: black, 1.1; white, 6.5), $|E_+(\vec{k})|^2$ (far field: white, 0; black, 0.02), $|E_-(x,y)|^2$ (near field: black, 0; white, 1.2), and $|E_-(\vec{k})|^2$ (far field: white, 0; black, 0.019). The far fields are drawn on logarithmic scales. The homogeneous mode ($k=0$) is in the center of the far field plots, and has been eliminated in all figures. Parameters: $I_0=3.92$, $\chi=78°$, and $\eta=1$.

For $\chi \rightarrow 0$, tongue II disappears, and tongue III is the only remaining region of instability. In Fig. 6(d), we plot the marginal stability curve for a right-handed circularly polarized input field ($\chi=0$). As discussed in Sec. II, this case is equivalent to the scalar case, already described in Refs. [26,27]. The steady state solution given by Eq. (7) is the same as the symmetric solution for a linearly polarized input, except for a rescaling of the intensities. After this rescaling, in the self-focusing case, the marginal stability curve is also the same as the one for linearly polarized input, and the same patterns are observed above threshold. In the self-defocusing case, however, we do not have any instability of the homogeneous solution. As stated in Sec. III, for a linearly polarized input field the self-defocusing instability involves the asymmetric modes. Here there is only one relevant component of the field, and there are not enough degrees of freedom for such an instability to occur.

V. MODIFIED HOPF BIFURCATION: DEFORMED DYNAMICAL HEXAGONS

In Fig. 9, we plot the squared absolute value of E_+ and E_- in the near and far fields for an input field intensity such that the value of I_{s+} is slightly above the threshold of the Hopf instability (region II) shown in Fig. 6(b). We can see that a distorted hexagonal structure appears for E_+ and E_-. The component E_- is correlated with E_+ but has a lower intensity because $\chi<90°$ gives preference to E_+. The structure has a dynamical evolution as shown in Fig. 10, where we plot four configurations of $|E_+|^2$ at different times. Inspection of the numerical results for the far field indicates

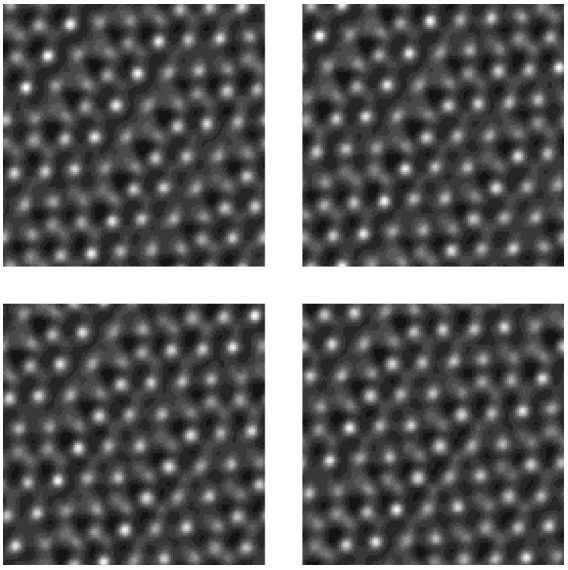

FIG. 10. Four configurations of $|E_+|^2$ during one period T of oscillation ($T=3.86$). From left to right and top to bottom, $t=0$, $t=0.97$, $t=1.93$, and $t=2.90$. The values of the parameters are the same as in Fig. 9. Gray scale values: a black, 1.1; white, 6.5.

that E_+ is dominated by a triad of three wave vectors with $|\vec{k}|=k_h$, while E_- is dominated by the triad with opposite wave vectors. In addition, we observe that these three wave vectors are not equivalent, since two of them, which form an angle close to 90°, carry a higher spectral power than the third one. The modes of E_+ with highest intensity are identified in Fig. 11. The two equivalent wave vectors are labeled $\vec{k}_2$ and $\vec{k}_3$, and the third dominant wave vector is labeled $\vec{k}_1$.

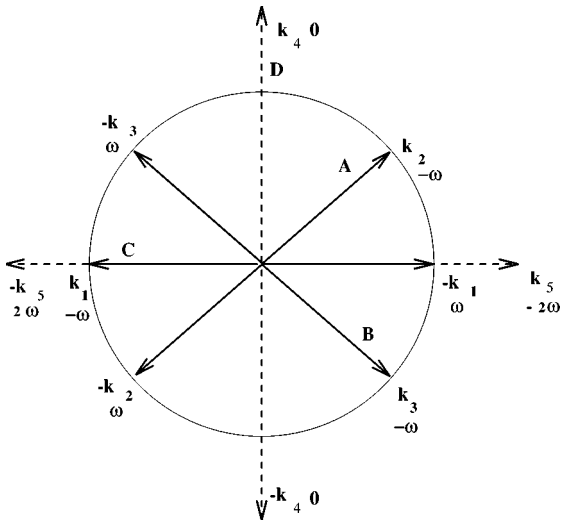

FIG. 11. Definition of the unstable Hopf and slaved stationary modes coupled through quadratic nonlinearities and described by the dynamical system (30). For asymptotic times, the modes k_1, k_2, and k_3, dominate and build the dynamical hexagons described in the text. The intensity range of these modes obtained from simulations [see $|E_+(\vec{k})|^2$ in Fig. 9] is from 0.0008 (damped static modes) to 0.019 (brightest Hopf mode).

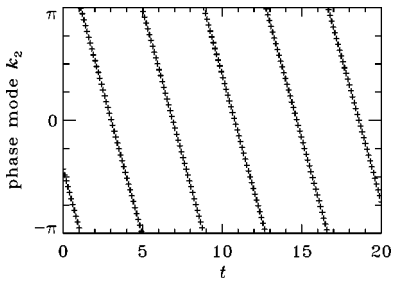

FIG. 12. Phase of the Hopf mode k_2 (see Fig. 11) as a function of time. The values of the parameters are the same as in Fig. 9. A period $T=3.86$ is obtained from the plot.

A basic feature of the dynamical evolution of the pattern can be understood considering the time evolution of each of these modes. The amplitude of any of these Hopf modes $|\vec{k}|=k_h$ evolves with a fixed frequency. The frequency has the same absolute value for all these modes but different signs, as indicated in Fig. 11. In Fig. 12, we display, as an example, the phase of the mode $\vec{k}_2$. The frequency obtained from this plot, $\omega=1.63$, coincides with the imaginary part of the critical eigenvalue associated with the Hopf instability.

Since the numerical results are obtained slightly above the instability threshold, we may hopefully interpret them in the framework of reduced dynamics and amplitude equations for the unstable modes. Let us first recall that we are dealing with a Hopf instability with broken translational symmetry. The real part of the most unstable eigenvalues λ_1 and λ_2 is plotted in Fig. 13. These eigenvalues are complex conjugated for $k \simeq k_h$ and $\lambda_{1,2}(k_h)=\pm i\omega$.

The field $E_\pm$ can be projected on the eigenvectors of the

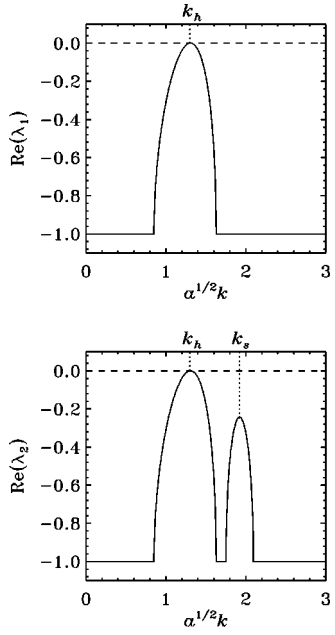

FIG. 13. Real part of most unstable eigenvalues λ_1 and λ_2. The values of the parameters are the same as in Fig. 9.

linear evolution matrix L and, using Eq. (8), may be written as

$$\begin{pmatrix} E_+ \\ E_+^* \\ E_- \\ E_-^* \end{pmatrix} = \begin{pmatrix} E_{s+} \\ E_{s+}^* \\ E_{s-} \\ E_{s-}^* \end{pmatrix} + \begin{pmatrix} E_{s+}\psi_+ \\ E_{s+}^*\psi_+^* \\ E_{s-}\psi_- \\ E_{s-}^*\psi_-^* \end{pmatrix} = \begin{pmatrix} E_{s+} \\ E_{s+}^* \\ E_{s-} \\ E_{s-}^* \end{pmatrix} + \sum_{\vec{k}} e^{i\vec{k}\cdot\vec{r}}(V_1\sigma_{1,\vec{k}} + V_2\sigma_{2,\vec{k}} + V_3\sigma_{3,\vec{k}} + V_4\sigma_{4,\vec{k}}), \tag{21}$$

where V_i are the four eigenvectors, in Fourier space, and $\sigma_{i,\vec{k}}$ are the corresponding amplitudes. The usual procedure of reducing the dynamics to the dynamics of the unstable modes only leads to the adiabatic elimination of the modes $V_3\sigma_{3,k}$ and $V_4\sigma_{4,k}$, because λ_3 and λ_4 are stable eigenvalues. Taking into account that the eigenvalues λ_1 and λ_2 are most unstable for $\vec{k}=\vec{k}_h$ with $|\vec{k}_h|=k_h$, we may write, close to the instability [3]

$$\begin{pmatrix} E_+ \\ E_+^* \\ E_- \\ E_-^* \end{pmatrix} = \begin{pmatrix} E_{s+} \\ E_{s+}^* \\ E_{s-} \\ E_{s-}^* \end{pmatrix} + \sum_{\vec{k}_h} (V_1\sigma_{1,\vec{k}_h}e^{i\vec{k}_h\cdot\vec{r}+i\omega t} + V_2\sigma_{2,\vec{k}_h}e^{i\vec{k}_h\cdot\vec{r}-i\omega t}) + \cdots . \tag{22}$$

The amplitudes, $\sigma_{1,\vec{k}_h}=\sigma_{1,\vec{k}_h}(\vec{X},T)$ and $\sigma_{2,\vec{k}_h}=\sigma_{2,\vec{k}_h}(\vec{X},T)$, only depend on the slow variables $\vec{X}=\varepsilon^{1/2}\vec{r}$ and $T=\varepsilon^{-1}t$, where $\varepsilon=(I_{s+}-I_{s+}^c)/I_{s+}^c$ is the reduced distance to the instability threshold (we are using I_{s+} as the bifurcation parameter, and I_{s+}^c is the critical value at the Hopf bifurcation). For each particular pattern, their evolution equations, or amplitude equations, may be derived with standard procedures [38]. However, it is often convenient instead to study order parameter equations of the Swift-Hohenberg type. These equations reduce to the correct amplitude equations near the onset of instability but take care of the orientational degeneracy of the unstable wave vectors, preserve the correct symmetries of the problem, allow the description of transitions between patterns of different symmetries, and contain rapid spatiotemporal variations which may be important for pattern selection or transient dynamics [3,35,39]. In the present case, we consider a model order parameter dynamics of the type

$$\partial_t\sigma_\pm = [\varepsilon - \xi_h^2(k_h^2+\nabla^2)^2 \pm i\omega]\sigma_\pm + v\,\sigma_\mp^2 - (1\pm i\beta)\sigma_\pm^2\sigma_\mp , \tag{23}$$

where the subscripts + and − refer to the sign of the frequency, so that the complex $\sigma_\pm$ are proportional to the wave packet $\sigma_{1(2),\vec{q}}\exp(i\vec{k}\cdot\vec{r}\pm i\omega t)$, with $|\vec{k}|\simeq k_h$. These equations contain quadratic nonlinearities, as discussed in Sec. II, and are thus equivalent to the equations describing oscillatory convection in hydrodynamic systems with no ''up-down'' symmetry [40]. In this case, the authors obtained monoperiodic regular states of hexagonal symmetry that correspond to a two-dimensional standing wave. We will call these states pulsating hexagons.

Our system has, however, the following originality. The eigenvalue λ_2 is real and only slightly negative for the modes σ_0 with a wave vector such that $|\vec{k}|=k_s\simeq\sqrt{2}k_h$ (see Fig. 13). As $k_s\simeq\sqrt{2}k_h$, the modes σ_0 may be coupled with pairs of Hopf modes $\sigma_\pm$ with orthogonal wave vectors via quadratic resonances. Since the modes σ_0 are only slightly damped, one should incorporate them in the order parameter dynamics, which then becomes

$$\begin{aligned} \partial_t\sigma_\pm &= [\varepsilon - \xi_h^2(k_h^2+\nabla^2)^2 \pm i\omega]\sigma_\pm + v_0\sigma_\mp^2 + v_1\sigma_\pm\sigma_0 \\ &\quad + v_2\sigma_0^2 - (1\pm i\beta)\sigma_\pm^2\sigma_\mp - (\gamma\pm i\delta)\sigma_0^2\sigma_\pm , \\ \partial_t\sigma_0 &= [\mu - \xi_s^2(k_s^2+\nabla^2)^2]\sigma_0 + \overline{v}_1\sigma_+\sigma_- + \overline{v}_2\sigma_0^2 - \sigma_0^3 \\ &\quad - u\sigma_0\sigma_+\sigma_- , \end{aligned} \tag{24}$$

where $\mu<0$ is the linear damping of the homogeneous mode [$\mu\propto\lambda_2(k_s)$]. The kinetic coefficients could be obtained numerically from Eq. (8). However, this formidable task may be avoided, since we are mainly interested in generic dynamical behaviors, which essentially depend on their signs and orders of magnitude.

Let us look for the possible asymptotic solutions of this system. Systems described by the dynamics (23) have been mainly studied in one-dimensional geometries where the resulting patterns correspond to traveling or standing waves [3,41,42]. These solutions are recovered here. Effectively, the uniform amplitude equations for critical unidirectional counterpropagating traveling waves corresponding to the modes $\sigma_0=0$, $\sigma_+=L\exp(i\vec{k}_h\cdot\vec{r}+i\omega t)+R^*\exp(-i\vec{k}_h\cdot\vec{r}+i\omega t)$ and $\sigma_-=L^*\exp(-i\vec{k}_h\cdot\vec{r}-i\omega t)+R\exp(i\vec{k}_h\cdot\vec{r}-i\omega t)$ ($|\vec{k}_h|=k_h$) may be deduced from Eq. (24), and are

$$\begin{aligned} \dot{L} &= \varepsilon L - (1+i\beta)L(|L|^2+2|R|^2), \\ \dot{R} &= \varepsilon R - (1-i\beta)R(|R|^2+2|L|^2). \end{aligned} \tag{25}$$

The nonlinear cross-coupling coefficients of the field equations are twice the self-coupling coefficients. In this situation, as in reaction-diffusion systems with scalar couplings [35], traveling waves are stable structures, whereas standing waves are unstable.

As we are considering two-dimensional systems, we have to study the stability of such waves versus modulations with wave vectors pointing in other directions. In the absence of coupling between $\sigma_\pm$ and σ_0, one should obtain pulsating hexagons, as in Ref. [40]. The coupling between oscillatory $\sigma_\pm$ and steady σ_0 modes may modify this picture, however. Effectively, let us consider the linear stability of a traveling wave defined by $\sigma_-=A\exp[ik_h(x+y)/\sqrt{2}-i\omega_0 t]$, $\sigma_+=A^*\exp[-ik_h(x+y)/\sqrt{2}+i\omega_0 t]$, with $|A|^2=\varepsilon$ and $\omega_0=\omega-\beta\varepsilon$, which corresponds to a solution of Eq. (25) with $L=0$ and $R=Ae^{i\beta\varepsilon t}$. (The wave vector direction is arbitrary, and we may choose this particular one, anticipating results of the following discussion. Based on the wave vector definition of Fig. 11, x and y being the spatial coordinates in the plane, the right traveling wave just described corresponds to mode A.) Mode A is quadratically coupled to the modes

$B\exp[ik_h(x-y)/\sqrt{2}-i\omega_0 t]$ and $De^{ik_s y}$ and their complex conjugates. Taking $\sigma_- = A\exp[ik_h(x+y)/\sqrt{2}-i\omega_0 t] + B\exp[ik_h(x-y)/\sqrt{2}-i\omega_0 t]$, $\sigma_+ = A^*\exp[-ik_h(x+y)/\sqrt{2}+i\omega_0 t]+B^*\exp[-ik_h(x-y)/\sqrt{2}+i\omega_0 t]$, and $\sigma_0 = De^{ik_s y}+D^*e^{-ik_s y}$, the corresponding linearized amplitude equations are of the forms

$$\dot{B} = -\varepsilon B + v_1 A D^* - \cdots,$$
$$\dot{D} = (\mu - u\varepsilon)D + \bar{v}_1 A B^* - \cdots. \tag{26}$$

The characteristic equation of the corresponding evolution matrix is

$$s^2 - s[(1+u)\varepsilon - \mu] + \varepsilon(u\varepsilon - \mu) - v_1\bar{v}_1\varepsilon = 0, \tag{27}$$

and the traveling waves are thus unstable for

$$\varepsilon < \varepsilon_c = \frac{1}{u}(v_1\bar{v}_1 + \mu). \tag{28}$$

If $v_1\bar{v}_1$ is negative, $\varepsilon_c < 0$, and unidirectional traveling waves are stable. This is, for example, the case in systems where the order parameter dynamics contains nonlinear couplings between the gradients of the field [43]. Alternatively, if $v_1\bar{v}_1$ is positive, and we may suppose that this is the case here, ε_c is positive when μ has a sufficiently small absolute value (we recall that $\mu<0$). Hence unidirectional traveling waves are unstable versus two-dimensional spatiotemporal patterns in the range $0<\varepsilon<\varepsilon_c$.

We will now try to identify these patterns, taking into account the fact that the dynamics favors propagating waves and contains quadratic nonlinearities. Hence, we consider that the dynamics may be reduced to the dynamics of the modes *A*, *B*, *C*, and *D* and their respective complex conjugates, as defined in Fig. 11. Starting with mode *A*, modes *B* and *D* should be included in the description, because *A* is unstable versus *B* and *D*. Mode *C* should also be included because of the coupling between *A* and *B*. The coupling between *A* and *B* also generates higher harmonics with frequency -2ω (vector $\vec{k}_5$ in Fig. 11), which can be observed in the far field shown in Fig. 9. However, since the dynamics of these harmonics is slaved to the dynamics of *A* and *B*, they are not considered here. The amplitude equations for modes *A*, *B*, *C*, and *D* obtained from Eq. (24), taking into account quadratic nonlinearities between wavy modes, are

$$\begin{aligned}
\partial_t A &= \varepsilon A + 4\xi_h^2(\vec{k}_2\cdot\vec{\nabla})^2 A + v_1 D B + v_0 C^* B^* e^{i(3\omega t+\kappa x)} \\
&\quad -(1+i\beta)A[|A|^2+2(|B|^2+|C|^2)] - (\gamma+i\delta)A|D|^2, \\
\partial_t B &= \varepsilon B + 4\xi_h^2(\vec{k}_3\cdot\vec{\nabla})^2 B + v_1 A D^* + v_0 C^* A^* e^{i(3\omega t+\kappa x)} \\
&\quad -(1+i\beta)B[|B|^2+2(|A|^2+|C|^2)] - (\gamma+i\delta)B|D|^2, \\
\partial_t C &= \varepsilon C + 4\xi_h^2(\vec{k}_1\cdot\vec{\nabla})^2 C + v_0 A^* B^* e^{i(3\omega t+\kappa x)} \\
&\quad -(1+i\beta)C[|C|^2+2(|B|^2+|A|^2)] - (\gamma+i\sigma)C|D|^2, \\
\partial_t D &= \mu D + 4\xi_s^2(\vec{k}_4\cdot\vec{\nabla})^2 D + \bar{v}_1 A B^* - \cdots,
\end{aligned} \tag{29}$$

where $\kappa = (1-\sqrt{2})k_h$. *D* may be adiabatically eliminated, and $D \simeq -\bar{v}_1 AB^*/\mu$. The mismatch between the modes *A*, *B*, and *C* may be absorbed in their phases ($\phi_i \to \bar{\phi}_i - \kappa x/3$). Writing $I = R_I\exp(\phi_I)$ and defining the total phase as $\Phi = \bar{\phi}_A + \bar{\phi}_B + \bar{\phi}_C - 3\omega t$, we finally obtain the following equations for uniform amplitudes and phases, up to cubic nonlinearities:

$$\begin{aligned}
\partial_t R_A &= \varepsilon_0 R_A + v_1 R_B R_C \cos\Phi - R_A(R_A^2 + \bar{\gamma}R_B^2 + 2R_C^2), \\
\partial_t R_B &= \varepsilon_0 R_B + v_1 R_A R_C \cos\Phi - R_B(R_B^2 + \bar{\gamma}R_A^2 + 2R_C^2), \\
\partial_t R_C &= \varepsilon_1 R_C + v_1 R_A R_B \cos\Phi - R_C[R_C^2 + 2(R_A^2+R_B^2)], \\
\partial_t \bar{\phi}_A &= -v_0 \frac{R_B R_C}{R_A}\sin\Phi + O(\beta,\delta,R^2), \\
\partial_t \bar{\phi}_B &= -v_0 \frac{R_A R_C}{R_B}\sin\Phi + O(\beta,\delta,R^2), \\
\partial_t \bar{\phi}_C &= -v_0 \frac{R_A R_B}{R_C}\sin\Phi + O(\beta,\delta,R^2), \\
\partial_t \Phi &= -3\omega - v_1 \frac{2R_C^2 + R_A^2}{R_C}\sin\Phi + O(\beta,\delta,R^2),
\end{aligned} \tag{30}$$

where $\varepsilon_0 = \varepsilon - \frac{2}{9}\xi_h^2(1-\sqrt{2})^2 k_h^4 \simeq \varepsilon - 0.038\xi_h^2 k_h^2$, $\varepsilon_1 = \varepsilon - \frac{4}{9}\xi_h^2(1-\sqrt{2})^2 k_h^4 \simeq \varepsilon - 0.075\xi_h^2 k_h^2$, and $\bar{\gamma} = 2 + v_2\bar{v}_1/\mu$. From these equations, it turns out that *A* and *B* are equivalent, $R_A = R_B \neq R_C$ and $\bar{\phi}_A - \bar{\phi}_B = \varphi$, where φ is an arbitrary constant. We may choose $\varphi = 0$ for simplicity.

Except for sufficiently small ω, where system (30) may admit fixed point solutions, this system of equations is expected to generate time-periodic solutions corresponding to pulsating deformed hexagons. Over a period, the mean value of the amplitude of the modes *A* and *B* should be equal, while the mean value of the amplitude of *C* should be smaller ($\varepsilon_1 < \varepsilon_0$, and $\bar{\gamma} < \gamma$). In the absence of coupling with the *D* mode ($\mu \ll 0$), one should recover the pulsating hexagons found by Brand and Deissler [40]. It is the particularity of this system to present a resonant interaction with a slowly evolving stable mode which induces the deformation of the hexagonal pattern. In general, *A* and B^* modes need not make a particular angle for their quadratic resonance with a stationary mode. If they make an angle ψ with the *Y* axis, they should be coupled with the stable *D* mode (with $k_s\hat{y} = 2k_h\sin\psi\hat{y}$, where $\hat{y}$ is the unit vector along the *Y* axis) in such a way that

$$\partial_t D(\psi) = [\mu - 4\xi_s^2(k_s^2 - 4\sin^2\psi k_h^2)^2]D(\psi) + \bar{v}_1 A B^* + \cdots. \tag{31}$$

Hence, the adiabatic elimination of this mode leads to a renormalized coefficient $\bar{\gamma}$ which is minimum for $\sin\psi = k_s/2k_h$. The angle ψ is then half of the selected angle between *A* and B^* wave vectors. Changing the detuning θ, the ratio between k_s and k_h can be tuned, which then changes the distortion of the hexagonal pattern.

If one now wishes to reconstruct the field from the results of this weakly nonlinear analysis, one obtains from Eqs. (22) and (30), at leading order,

$$\begin{pmatrix} E_+ \\ E_+^* \\ E_- \\ E_-^* \end{pmatrix} - \begin{pmatrix} E_{s+} \\ E_{s+}^* \\ E_{s-} \\ E_{s-}^* \end{pmatrix} = \sum_{\vec{k}_h} \left(V_1 \sigma_{1,\vec{k}_h} e^{i\vec{k}_h\cdot\vec{r}+i\omega t} + V_2 \sigma_{2,\vec{k}_h} e^{i\vec{k}_h\cdot\vec{r}-i\omega t} \right) + \cdots$$

$$= V_1 e^{i\omega t}(A^* e^{-i\vec{k}_2\cdot\vec{r}} + B^* e^{-i\vec{k}_3\cdot\vec{r}} + C^* e^{-i\vec{k}_1\cdot\vec{r}}) + V_2 e^{-i\omega t}(A e^{i\vec{k}_2\cdot\vec{r}} + B e^{i\vec{k}_3\cdot\vec{r}} + C e^{i\vec{k}_1\cdot\vec{r}}) + \cdots$$

$$= V_1 e^{i\omega t}\left(2R_A \cos\frac{k_h y}{\sqrt{2}} e^{-i(k_h x/\sqrt{2}) - i\bar{\phi}_A} + R_C e^{ik_h x - i\bar{\phi}_C} \right)$$

$$+ V_2 e^{-i\omega t}\left(2R_A \cos\frac{k_h y}{\sqrt{2}} e^{i(k_h x/\sqrt{2}) + i\bar{\phi}_A} + R_C e^{-ik_h x + i\bar{\phi}_C} \right) + \cdots . \quad (32)$$

From Eq. (30), it may be seen that $\bar{\phi}_A$ and $\bar{\phi}_C$ are functions of Φ. Since ω is finite, close to the instability threshold one may expand Φ around $3\omega t$ [44], and Eq. (32) becomes

$$\begin{pmatrix} E_+ \\ E_+^* \\ E_- \\ E_-^* \end{pmatrix} - \begin{pmatrix} E_{s+} \\ E_{s+}^* \\ E_{s-} \\ E_{s-}^* \end{pmatrix} = V_1 e^{i\omega t}\left(2R_A \cos\frac{k_h y}{\sqrt{2}} e^{-i(k_h x/\sqrt{2})} + R_C e^{ik_h x} \right) + V_2 e^{-i\omega t}\left(2R_A \cos\frac{k_h y}{\sqrt{2}} e^{i(k_h x/\sqrt{2})} + R_C e^{-ik_h x} \right) + \cdots , \quad (33)$$

where R_A and R_B still contain time-dependent contributions of frequencies $3\omega, 6\omega, \ldots$. The corresponding spatiotemporal patterns are thus different from pulsating hexagons, since, besides their deformation, they are built on a triad of traveling waves propagating in the $\vec{k}_1$, $\vec{k}_2$, and $\vec{k}_3$ (or $-\vec{k}_1, -\vec{k}_2$, and $-\vec{k}_3$) directions, leading to what we call deformed dynamical hexagons. These conclusions are in qualitative agreement with the numerical results presented in Figs. 9, 10 and 12, which tell us, furthermore, that the eigenvectors V_1 and V_2 should have dominant contributions to E_+ and E_-, respectively. Effectively, it appears that the dominant contributions to E_- come from the modes k_1, k_2, and k_3 with frequency $-\omega$, while E_+ is built on the modes k_1, k_2, and k_3, with frequency ω.

We thus think that the main feature which determines the properties of the patterns presented in Figs. 9 and 10 is the fact that a constructive coupling occurs between a nearly marginal stationary mode and unstable oscillatory modes. Couplings between steady and oscillatory modes have already been shown to be able to induce subharmonic Hopf bifurcations in one-dimensional reaction-diffusion systems in codimension 2 situations [45,46]. Here this particular coupling is allowed by the two-dimensional geometry of the system, which induces the bifurcation to spatiotemporal patterns with deformed hexagonal shape.

VI. CODIMENSION 2 HOPF AND TURING-LIKE INSTABILITIES

In this section, we consider the situation shown in Figs. 2(c) (steady state) and 6(c) (marginal stability), corresponding to an ellipticity $\chi=73°$ and detuning $\theta=1$. We see from the marginal stability curve that there are two different wave numbers that become unstable at nearly the same value of the control parameter I_{s+}. Similar situations can be obtained changing simultaneously the ellipticity and the detuning. For example, for $\chi=67°$ and $\theta=0.6$ the same type of situation occurs (the relation between the two critical wave numbers changes but the qualitative results are not affected). In Fig. 14, we plot the unstable eigenvalues λ_1 and λ_2 as functions of the wave number k near the instability threshold for $\chi=67°$ and $\theta=0.6$. In the plot of λ_2 we can see that the modes k_h and k_s become simultaneously unstable, and, furthermore, $\lambda_2(k_h)$ is complex, while $\lambda_2(k_s)$ is real. Hence, we have a codimension 2 situation where the oscillatory instability corresponding to a Hopf bifurcation with broken spatial symmetry and the stationary Turing-like instability are close together. In Fig. 15, we show numerical results for the near and the far fields of E_+ at three different times during the transient following this codimension 2 bifurcation. These results display the competition between the Hopf and the static modes. At short times the Hopf modes dominate, but at long times a static hexagonal pattern is formed.

In the vicinity of the codimension two point, the field variables may be written as

$$\begin{pmatrix} E_+ \\ E_+^* \\ E_- \\ E_-^* \end{pmatrix} = \begin{pmatrix} E_{s+} \\ E_{s+}^* \\ E_{s-} \\ E_{s-}^* \end{pmatrix} + \sum_{\vec{k}_h} \left(V_1 \sigma_{1,\vec{k}_h} e^{i\vec{k}_h\cdot\vec{r}+i\omega t} + V_2 \sigma_{2,\vec{k}_h} e^{i\vec{k}_h\cdot\vec{r}-i\omega t} \right) + \sum_{\vec{k}_s} V_3 \sigma_{0,k_s} e^{i\vec{k}_s\cdot\vec{r}}, \quad (34)$$

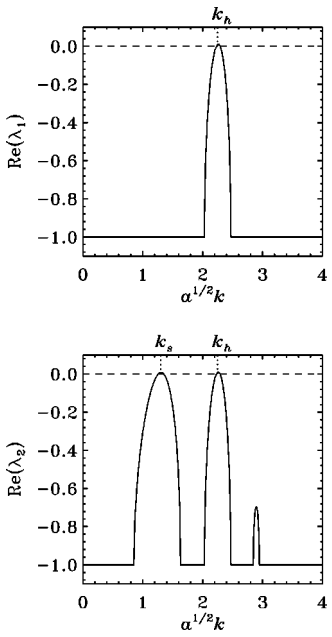

FIG. 14. Real part of unstable eigenvalues λ_1 and λ_2. Parameters: $I_0=10.9$, $\chi=67°$, and $\eta=1$.

where $|\vec{k}_h|=k_h$ and $|\vec{k}_s|=k_s$ are the critical wave numbers associated with each of the instabilities mentioned before. This expansion is the generalization of Eq. (22) to the codimension 2 situation, where one has to expand the fields on all the unstable modes of the problem, including here the Turing-like unstable mode. The amplitudes $\sigma_{1,\vec{k}_h}(\vec{X},T)$, $\sigma_{2,\vec{k}_h}(\vec{X},T)$ and $\sigma_{0,\vec{k}_s}(\vec{X},T)$ only depend on the slow variables of the problem $\vec{X}=\varepsilon^{1/2}\vec{x}$ and $T=\varepsilon^{-1}t$. Furthermore, we define μ as the reduced distance to the stationary instability threshold [$\mu=(I_{s+}-I_{s+}^c)/I_{s+}^c$, where now I_{s+}^c is the critical value of the bifurcation parameter at this Turing-like instability; μ is positive, contrary to the case discussed in the Sec. V.]

The structure of the evolution equations for these amplitudes may easily be obtained using the symmetries of the problem [38]. Contrary to the case discussed in Sec. V, in the present situation $k_s<k_h$, so that there should be no quadratic couplings between oscillatory hexagonal planforms and steady modes. In the absence of such resonances, oscillatory and stationary modes are first coupled through cubic nonlinearities. For example, the dynamics of a pair of unidirectional counterpropagating traveling waves of amplitudes A and B, coupled to an arbitrary number of steady modes of amplitudes R_i correspond to the following coupled Ginzburg-Landau and Swift-Hohenberg equations:

$$\begin{aligned}
\partial_t A &= \mathcal{E}_{\mathrm{GL}_A}(\varepsilon,A,B)-g(1+id)A\Sigma_i|R_i|^2,\\
\partial_t B &= \mathcal{E}^*_{\mathrm{GL}_B}(\varepsilon,A,B)-g(1-id)B\Sigma_i|R_i|^2,\\
\partial_t R_i &= \mathcal{E}_{\mathrm{SH}_i}(R_j)-wR_i(|A|^2+|B|^2),
\end{aligned} \tag{35}$$

where, in the absence of mean flow or group velocity, $\mathcal{E}_{\mathrm{GL}_A}(\varepsilon,A,B)=\varepsilon A+(1+i\alpha)\partial_x^2 A-(1+i\beta)A(|A|^2+\gamma|B|^2)$, with $\vec{k}_h\|\hat{x}$. $\mathcal{E}_{\mathrm{SH}_i}(R_j)$ represents the generic evolution terms of

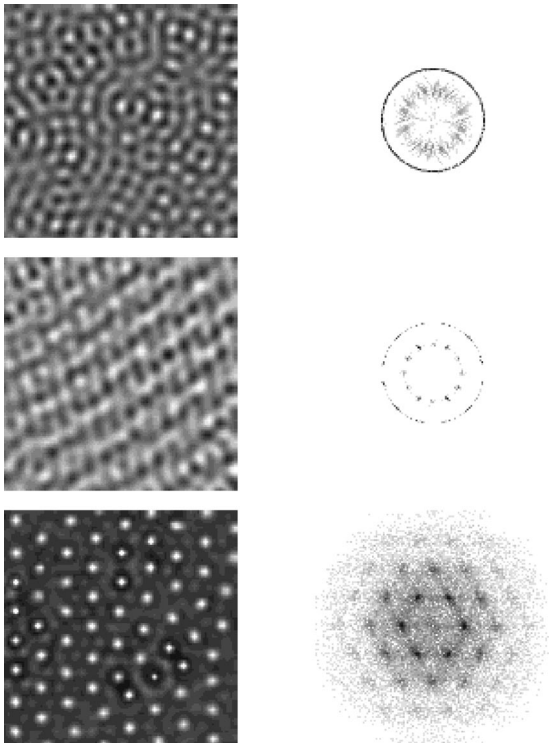

FIG. 15. Near field [$|E_+(x,y)|^2$] and far field [$|E_+(\vec{k})|^2$, on a logarithmic scale) at three different times for the Turing-Hopf competition. From top to bottom, $t=50$ (near field: black, 3.6; white, 7.1; far field: white, 0; black, 5.3×10^{-4}), $t=700$ (near field: black, 4.6; white, 5.5; far field: white, 0; black, 2.1×10^{-4}), and $t=1700$ (near field: black, 0.6; white, 16; far field: white, 0; black, 0.039). The values of the parameters are the same as in Fig. 14.

the Swift-Hohenberg type close to a Turing-like instability. In the absence of ''up-down'' symmetry, as it is the case here, quadratic nonlinear couplings between stationary modes are important. The corresponding dynamical operator may then be written, for an arbitrary triad of modes, as ($i,j=1,2,3$)

$$\begin{aligned}
\mathcal{E}_{\mathrm{SH}_1}(R_j) &= \mu R_1+(\vec{k}_{s1}\cdot\vec{\nabla})^2R_1+vR_2^*R_3^*-|R_1|^2R_1\\
&\quad -u(|R_2|^2+|R_3|^2)R_1,\\
\mathcal{E}_{\mathrm{SH}_2}(R_j) &= \mu R_2+(\vec{k}_{s2}\cdot\vec{\nabla})^2R_2+vR_1^*R_3^*-|R_2|^2R_2\\
&\quad -u(|R_1|^2+|R_3|^2)R_2,\\
\mathcal{E}_{\mathrm{SH}_3}(R_j) &= \mu R_3+(\vec{k}_{s3}\cdot\vec{\nabla})^2R_3+vR_1^*R_3^*-|R_3|^2R_3\\
&\quad -u(|R_2|^2+|R_1|^2)R_3,
\end{aligned} \tag{36}$$

with $\vec{k}_{s1}+\vec{k}_{s2}+\vec{k}_{s3}=\vec{0}$. Since we are dealing with a system with scalar non linear couplings, γ, u, g, and w should be larger than one.

Codimension 2 situations have been extensively studied in one-dimensional reaction-diffusion systems where Turing and zero-wave number Hopf instability thresholds are close together [35,45,46]. According to the nonlinear couplings between unstable modes, the resulting patterns may be pure Turing, pure Hopf, or mixed mode patterns. We are considering here two-dimensional geometries and a Hopf bifurca-

tion with finite wave vector. Equations (35) and (36) admit as steady states pure stripes of amplitude $\sqrt{\mu}$ or hexagonal planforms, where $R_i = R_0$ and $A = B = 0$, with

$$R_0 = \frac{v + \sqrt{v^2 + 4(1+2u)\mu}}{2(1+2u)}.$$

Stripes are unstable versus hexagons for $\mu < v^2/(u-1)^2$, which is expected to be the case here since v is finite and $\mu \ll 1$. They also admit as asymptotic solutions traveling waves (of amplitude $|A| = |A_0| = \sqrt{\varepsilon}$, $B = 0$, $R = 0$ or $|B| = |B_0| = \sqrt{\varepsilon}$, $A = 0$, $R = 0$) and mixed modes.

The stability of hexagonal patterns versus wavy modes may be studied with the following linearized equations:

$$\begin{aligned} \partial_t A &= \varepsilon A + (1 + i\alpha)\partial_x^2 A - 3g(1+id)|R_0|^2 A, \\ \partial_t B &= \varepsilon B + (1 + i\alpha)\partial_x^2 B - 3g(1+id)|R_0|^2 B. \end{aligned} \tag{37}$$

The result is that hexagonal planforms are stable for

$$\varepsilon < \frac{3g}{2(1+2u)}[v + \sqrt{v^2 + 4(1+2u)\mu}], \tag{38}$$

which is the case to be expected here since ε is small and v finite.

Since we suppose that γ is larger than 1, the pure wavy solutions of Eq. (35) are traveling waves of amplitude $\sqrt{\varepsilon}$. The evolution of the steady modes R_i in the presence of pure traveling waves ($|A_0| = \sqrt{\varepsilon}$, $|B_0| = 0$ or $|B_0| = \sqrt{\varepsilon}$, $|A_0| = 0$) is given by

$$\partial_t R_i = \mathcal{E}_{\mathrm{SH}_i}(R_j) - w\varepsilon R_i. \tag{39}$$

Traveling waves are then linearly stable if $\mu - w\varepsilon < 0$, which should be the case here. Hence, for the situation discussed in this section, hexagonal and wave patterns are expected to be simultaneously stable.

The condition for the existence of mixed hexagon-traveling wave modes is found to be

$$1 + 2u > 3gw, \tag{40}$$

and is not expected to be satisfied in reaction-diffusion dynamics with scalar nonlinear couplings.

It is important to note that the Hopf bifurcation is supercritical, while the Turing-like transition to hexagons is subcritical. As a result of their supercriticality, wavy patterns grow first. Although these patterns are linearly stable versus stationary hexagonal planforms, the dynamics of the latter present destabilizing quadratic nonlinearities. The result is that the hexagonal patterns grow faster and finally take over. Since steady hexagons are stable versus waves, they should thus be the final pattern, although wave patterns may appear as transients during the first part of the evolution. This is indeed what is observed in the numerical simulations of Fig. 15: at time $t = 50$, there is a dominance of Hopf modes with arbitrary orientations with weakly excited Turing modes, as clearly seen in the far field. At late times ($t = 1700$) the Hopf modes have lost the competition, and only Turing modes giving an hexagonal pattern survive. Complicated dynamical competition occurs at intermediate times. In Fig. 16, we show the integrated power of Hopf and Turing modes as functions of time. The Hopf modes are seen to grow supercritically first, but eventually the subcritical Turing modes grow faster until they overcome the Hopf modes.

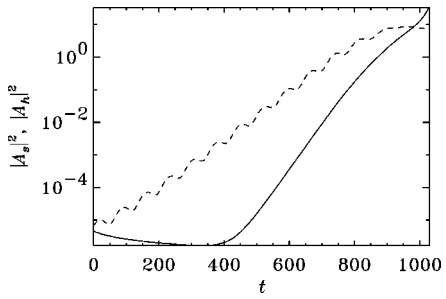

FIG. 16. Time dependence of the amplitudes $|A_s|^2$ (solid line) and $|A_h|^2$ (dashed line), corresponding to wave numbers k_s and k_h on a logarithmic scale. The amplitudes were calculated integrating over a circle of radius k_s or k_h in Fourier space. The plot shows the exponential growth of the Hopf modes at short times, the competition between the modes and the final domination of the static modes.

VII. SUMMARY AND DISCUSSION OF RESULTS

In previous sections we have reported a rich phenomenology for the broad range of values of the cavity detuning ($2/B - 1 < \theta < \sqrt{3}$) that we have explored. Here we summarize these results, and discuss their connection to other related studies. In Sec. III we revisited the case of linearly polarized driving field for self-focusing as well as self-defocusing situations. For the self-defocusing case there is an instability leading to a stripe stationary pattern which is orthogonally polarized to the driving field [18]. However, increasing the intensity of the driving field, the pattern disappears, leading to a final homogeneous elliptically polarized state. The transient dynamics involves the spatial coexistence of two equivalent elliptically polarized homogeneous states separated by moving interfaces, like in a process of phase separation dynamics [47]. Spatial coexistence of domains of different structures was reported in Ref. [48] for a liquid crystal light valve with rotated feedback loop, while stationary spatial coexistence of circularly polarized states has been reported in alkali vapors driven by a linearly polarized field in a single mirror system [22] and in cells without mirrors [20,21]. For a linearly polarized driving field and a self-focusing situation, there is an instability leading to an hexagonal pattern with the same polarization of the driving field [18]. This is the same process as in a scalar model [26,27]. When the intensity of the driving field is increased, the hexagonal pattern is destabilized [31]. We have observed that a further increase of the driving field intensity leads to a complicated spatiotemporal dynamics with bursting spots that create propagating circular waves. A related phenomenon was reported in a model which includes the dynamics of atomic variables [49].

For an elliptically polarized driving field (Sec. IV) and a self-defocusing situation, the stripe pattern is converted into a hexagonal pattern in each of the two independent vectorial components of the electric field. A transition from bright to dark hexagons (or vice versa) in each of the field components is obtained by changing the ellipticity of the driving field. In

addition, the range of parameters (cavity detuning and input intensity) for which a pattern exists shrinks to zero as the ellipticity departs from its value for a linearly polarized driving field. Beyond a certain ellipticity, the homogeneous solution, which now is elliptically polarized, never loses stability. The change from stripes or squares to hexagons for any finite ellipticity follows from general symmetry considerations also made in Ref. [34] for a Kerr medium with counterpropagating beams. This has been predicted [19] and observed [23] in a Na cell with single feedback mirror. It has also been invoked as an explanation of the observations in Ref. [24] for a cell of rubidium vapor in two counterpropagating beams. The transition from bright to dark hexagons by changing the ellipticity of a driving field was discussed in Ref. [36] and observed in Ref. [23] for Na vapor with a single feedback mirror.

For an elliptically polarized driving field and a self-focusing situation, the field ellipticity is a tuning parameter that permits one to explore several situations. For a circularly polarized driving field the scalar case is recovered, and a circularly polarized hexagonal pattern emerges. Two particularly interesting cases for intermediate ellipticity involve dynamical patterns occurring through a Hopf instability at a finite wave number k_h. The first of these instabilities considered in Sec. V leads to a time dependent pattern consisting of deformed dynamical hexagons. The Hopf bifurcation is modified by a linearly damped stationary mode $k_s > k_h$. The quadratic resonance of these two modes gives rise to deformed hexagons. The spatiotemporal pattern can be described by a superposition of a triad of k_h Hopf modes, each one associated with a traveling wave with the same frequency, but one of them having an amplitude different from the other two. A second interesting case considered in Sec. VI is a codimension 2 bifurcation in which a stationary Turing-like instability occurs simultaneously with the Hopf instability. Now the stationary unstable mode is such that $k_h > k_s$, and we do not find quadratic resonance. The transient dynamics involves complicated states with a strong competition of the Hopf and stationary modes. The final state is a stationary hexagonal pattern in which the Hopf modes have died. Dynamical patterns and codimension Turing-Hopf bifurcations have been considered in related studies. A first case of dynamical hexagons, in a Kerr medium with counterpropagating beams, was discussed in [34], but they arise as a secondary pure Hopf instability. Dynamical hexagons arising from a codimension 2 situation, for alkali vapors with a single feedback mirror, were considered in Refs. [50,51]. The difference from the situations we have found is twofold. First, the codimension 2 situation is different from ours because $k_s > k_h$, so that a mixed Turing-Hopf mode occurs through a quadratic resonances. Second, the dynamical pattern of Refs. [50,51] is different from our deformed dynamical hexagons because the Turing-like mode is linearly unstable and therefore appears with a large amplitude. In spite of these differences, we note that the deformation of hexagons in Ref. [51] has an origin similar to ours. The competition of unstable Hopf modes and unstable Turing-like modes with $k_s > k_h$ was also considered experimentally in Ref. [48] for a large system. By an appropriate control of parameters, either of the two types of modes can dominate. Close to the codimension 2 situation, the spatial coexistence of domains in which one of the two modes dominates was observed [52]. A codimension 2 bifurcation involving a Turing-like mode and a Hopf mode, but of zero wave number ($k_h = 0$), was also recently considered in an optical parametric oscillator with saturable losses [54].

VIII. CONCLUSIONS

In this paper we have presented a systematic analysis of a prototype vectorial model of pattern formation in nonlinear optics describing a Kerr medium in a cavity with flat mirrors and driven by a coherent plane-wave field. We have considered linearly as well as elliptically polarized driving fields, and situations of self-focusing and self-defocusing. We have described, by numerical simulations, amplitude and model equations, a rich variety of phenomena that illustrate the relevance of the polarization degree of freedom in optical spatiotemporal dynamics. In particular, we have shown that this degree of freedom allows for new asymmetric homogeneous solutions, induces new instabilities, and changes the basic symmetry of the pattern formed beyond an instability.

A particularly relevant aspect of our results is to show that the ellipticity of the pump can be used as a tuning parameter, easily accessible to the experimentalist, that permits one to explore different types of pattern forming instabilities. For example, we have shown that by changing the ellipticity we find situations which include (i) a modified Hopf bifurcation at a finite wave number leading to a time dependent pattern of deformed hexagons, and (ii) a codimension 2 Turing-Hopf instability resulting in an elliptically polarized stationary hexagonal pattern. Small changes in the ellipticity also change the symmetry of the pattern, for example from stripes to hexagons. Another general relevant aspect of our results is that the information on two different patterns is encoded in each of the two independent polarization components, which are easily separated by a polarizer. From a fundamental point of view this opens the possibility to study spatiotemporal correlations between two different patterns emerging from the same physical system [14]. Correlations between different polarization components close to the onset of pattern formation in the model of Ref. [18] were already studied in Ref. [28].

We finally mention that vectorial degrees of freedom are also important in pattern formation in lasers, where vectorial topological defects of the field amplitude can occur if the rotational symmetry of the system is not broken by a pump field [12,17,55,56]. Corresponding phenomena should also exist in other fields such as two-component Bose-Einstein condensates [4]. This calls for a further systematic investigation of vectorial spatiotemporal phenomena, for which a number of experimental results are becoming available.

ACKNOWLEDGMENTS

We want to acknowledge interesting discussions with Dr. M. Santagiustina. We also acknowledge Dr. A. Vicens for a careful reading of the manuscript. This work was supported by QSTRUCT (Project No. ERB FMRX-CT96-0077). Financial support from DGICYT (Spain), Project No. PB94-1167, is also acknowledged. M.H. wants to acknowledge financial support from the FOMEC project 290, Dep. de Física FCEyN, Universidad Nacional de Mar del Plata, Argentina.

[1] *Nonlinear Optical Structures, Patterns, Chaos*, edited by L. A. Lugiato, special issue of Chaos Solitons Fractals **4**, 1251 (1994), and references therein.
[2] D. Alessandro and W. J. Firth, Phys. Rev. Lett. **66**, 2597 (1991); Phys. Rev. A **46**, 537 (1992).
[3] M. C. Cross and P. C. Hohenberg, Rev. Mod. Phys. **65**, 851 (1993).
[4] Th. Busch, J. I. Cirac, V. M. Perez-Garcia, and P. Zoller, preprint, cond-mat/9712123.
[5] M. Kitano, T. Yabuzaki, and T. Ogawa, Phys. Rev. Lett. **46**, 926 (1981).
[6] M. I. Zheludev, Usp. Fiz. Nauk **157**, 683 (1989) [Sov. Phys. Usp. **32**, 357 (1989)].
[7] G. P. Puccioni, M. V. Tratnik, J. E. Sipe, and G. L. Oppo, Opt. Lett. **12**, 242 (1987).
[8] N. B. Abraham, M. San Miguel, and E. Arimondo, Opt. Commun. **117**, 344 (1995); **121**, 168 (1995).
[9] N. B. Abraham, M. D. Matlin, and R. S. Gioggia, Phys. Rev. A **53**, 3514 (1996).
[10] C. Serrat, A. Kulminskii, R. Vilaseca, and R. Corbalan, Opt. Lett. **20**, 1353 (1995).
[11] M. San Miguel, Phys. Rev. Lett. **75**, 425 (1995).
[12] L. Gil, Phys. Rev. Lett. **70**, 162 (1993).
[13] A. Amengual, D. Walgraef, M. San Miguel, and E. Hernández-García, Phys. Rev. Lett. **76**, 1956 (1996).
[14] A. Amengual, E. Hernández-García, R. Montagne, and M. San Miguel, Phys. Rev. Lett. **78**, 4379 (1997).
[15] C. Taggiasco, R. Meucci, and N. B. Abraham, Opt. Commun. **133**, 507 (1997).
[16] J. Martin Regalado, S. Balle, and M. San Miguel, Opt. Lett. **22**, 460 (1997).
[17] F. Prati, G. Tissoni, M. San Miguel, and N. B. Abraham, Opt. Commun. **143**, 133 (1997).
[18] J. B. Geddes, J. V. Moloney, E. M. Wright, and W. J. Firth, Opt. Commun. **111**, 623 (1994).
[19] A. J. Scroggie and W. J. Firth, Phys. Rev. A **53**, 2752 (1996).
[20] A. C. Tam and W. Happer, Phys. Rev. Lett. **38**, 278 (1977).
[21] A. Gahl, J. Seipenbusch, A. Aumann, M. Möller, and W. Lange, Phys. Rev. A **50**, R917 (1994).
[22] G. Grynberg, A. Maitre, and A. Petrossian, Phys. Rev. Lett. **72**, 2379 (1994).
[23] A. Aumann, E. Büthe, Yu. A. Logvin, T. Ackemann, and W. Lange, Phys. Rev. A **56**, R1709 (1997).
[24] A. Maitre, A. Petrossian, A. Blouin, M. Pinard, and G. Grynberg, Opt. Commun. **116**, 153 (1995).
[25] J. V. Moloney and H. M. Gibbs, Phys. Rev. Lett. **48** 1607, (1982); A. Quarzeddini, H. Adachihara, and J. V. Moloney, Phys. Rev. A **38**, 2005 (1988).
[26] L. A. Lugiato and R. Lefever, Phys. Rev. Lett. **58**, 2209 (1987).
[27] W. J. Firth, A. J. Scroggie, G. S. McDonald, and L. Lugiato, Phys. Rev. A **46**, R3609 (1992).
[28] M. Hoyuelos, P. Colet, and M. San Miguel, Phys. Rev. E (to be published).
[29] In Ref. [18], I_0 is defined as the intensity of any of the components of the input field, so in the equivalent equation in Ref. [18] I_0 is not divided by 2.
[30] The numerical scheme used for integration of Eq. (1) was described in detail by R. Montagne, E. Hernández-García, A. Amengual, and M. San Miguel, Phys. Rev. E **56**, 151 (1997). The method is pseudospectral and second order accurate in time, and is similar to the so-called two-step method. Lattices of size 128×128 were used.
[31] A. J. Scroggie, W. J. Firth, G. S. McDonald, M. Tlidi, R. Lefever, and L. A. Lugiato, Chaos Solitons Fractals **4**, 1323 (1994).
[32] See, for example, K. Rypdal and J. J. Rasmussen, Phys. Scr. **33**, 498 (1986).
[33] M. V. Goldman, K. Rydal, and B. Hafizi, Phys. Fluids **23**, 945 (1980).
[34] J. B. Geddes, R. A. Indik, J. V. Moloney, and W. J. Firth, Phys. Rev. A **50**, 3471 (1994).
[35] P. Borckmans, G. Dewel, A. De Wit, and D. Walgraef, in *Chemical Waves and Patterns*, edited by R. Kapral and K. Showalter (Kluwer, Dordrecht, 1994), pp. 323–363.
[36] T. Ackemann, Y. A. Logvin, A. Heuer, and W. Lange, Phys. Rev. Lett. **75**, 3450 (1995).
[37] Q. Ouyang, G. H. Gunaratne, and H. L. Swinney, Chaos **3**, 707 (1993).
[38] D. Walgraef, *Spatio-Temporal Pattern Formation* (Springer-Verlag, New York, 1996).
[39] P. Manneville, *Dissipative Structures and Weak Turbulence* (Academic, San Diego, 1990).
[40] H. R. Brand and R. J. Deissler, Phys. Lett. A **231**, 179 (1997).
[41] M. Bestehorn and H. Haken, Phys. Rev. A **42**, 7195 (1990).
[42] H. R. Brand, P. S. Lomdahl, and A. C. Newell, Physica D **23**, 345 (1986).
[43] C. A. Jones and M. R. E. Proctor, Phys. Lett. A **121**, 224 (1987); M. R. E. Proctor and C. A. Jones, J. Fluid Mech. **188**, 301 (1988).
[44] Y. Kuramoto, *Chemical Oscillations, Waves and Turbulence* (Springer-Verlag, Berlin, 1984).
[45] D. Lima, A. De Wit, G. Dewel, and P. Borckmans, Phys. Rev. E **53**, R1305 (1996).
[46] A. De Wit, D. Lima, G. Dewel, and P. Borckmans, Phys. Rev. E **54**, 261 (1996).
[47] J. D. Gunton, M. San Miguel and P. Sahni, in *Phase Transitions and Critical Phenomena*, edited by C. Domb and J. Lebowitz (Academic, New York, 1983), Vol. 8.
[48] S. Residori, P. L. Ramazza, E. Pampaloni, S. Boccaletti, and F. T. Arecchi, Phys. Rev. Lett. **76**, 1063 (1996).
[49] M. Le Berre, A. S. Patrascu, E. Ressayre, and A. Tallet, Phys. Rev. A **56**, 3150 (1997).
[50] Y. A. Logvin, T. Ackemann and W. Lange, Europhys. Lett. **38**, 583 (1997).
[51] Y. A. Logvin, B. A. Samson, A. A. Afanas'ev, A. M. Samson, and N. A. Loiko, Phys. Rev. E **54**, R4548 (1996).
[52] After the completion of this work, we learned of a theoretical study [53] of the experiments in Ref. [51] and other related situations. The authors of Ref. [53] considered a quadratic resonance of a Turing-like mode, and two Hopf modes of finite wave number in a manner similar to our analysis of the deformed dynamical hexagons.
[53] L. M. Pismen and B. Y. Rubinstein (unpublished).
[54] M. Tlidi, P. Mandel, and M. Haelterman, Phys. Rev. E **56**, 6524 (1997).
[55] L. Pismen, *Vortices in Nonlinear Fields* (Oxford University Press, London, 1998).
[56] M. Hoyuelos, E. Hernández-García, P. Colet, and M. San Miguel (unpublished).
[57] M. Hoyuelos, D. Walgraef, P. Colet, and M. San Miguel (unpublished).